Journal of Mines, Metals and Fuels, *73(9): 2759-2769; 2025. DOI: 10.18311/jmmf/2025/49186*

Print ISSN : 0022-2755

Journal of Mines, Metals and Fuels

Contents available at: *www.informaticsjournals.co.in/index.php/jmmf*

High Temperature Corrosion Studies X-ray Detraction Analysis on GTA Welded Dissimilar Metals of Inconel 718 and ASS 316

K. Balaji[1], K. Brahma Raju[2] and K. Venkata Subbaiah[3]

[1]Department of Mechanical Engineering, VSM College of Engineering, Ramachandrapuram - 533255, Andra Pradesh, India; balaji9182020681@gamil.com

[2]Department of Mechanical Engineering, S.R.K.R. Engineering College,Bhimavaram - 534204, Andra Pradesh, India

[3]Department of Mechanical Engineering, University College of Engineering, Andhra University, Visakhapatnam - 530003, Andhra Pradesh, India

Abstract

Oxidation and hot corrosion are major problems in marine, aircraft industries, petrochemical, thermal power plants, boiler part pressure vessel and land-based gas turbines etc. The surfaces of metals and alloys in oxidizing environments at high temperatures sometimes experience accelerated oxidation when they are covered with a thin fused salt layer. Due to the use of a wide range of tubes, increased operating temperatures can cause deterioration of the turbines. Inconel 718 and ASS 316 super-alloys (medium grade) are used as important materials for high-temperature conditions to avoid the problems of super-alloys. In the current research, the Inconel 718 and Austenitic Stainless Steel (ASS) 316 (3 mm thick) are welded by using the GTAW process has conducted oxidation and hot corrosion studies are conducted on weldments. The Weldments and parenting were studied in the presence of air and molten salt climate (Na_2SO_4+V_2O_5). Air and molten salt studies were conducted in the laboratory furnace for 50 iterations, with 1-hour heating at 9500c, 10500c and 11500c in each cycle, then 20 minutes of cooling. The samples are critically examined and the change in weight is recorded at the end of each cycle.In the case of studies in molten salt environments, after heating the sample at 2000C, a uniform layer (3-5mg/cm^2) of Na2SO_4+V_2O_5 mixture is coated on the samples with the help of a camel hair brush. The chemical composition and morphologies of the oxide scales were confirmed using X-ray diffraction analysis. The oxidation resistance is not only related to the nature of the passivation film and also depends on the salt environment and the structure of the alloy. This hardness difference is caused by the formation of carbides during the welding thermal cycle. In environmental studies, TIG welding of molten salt (Na_2SO_4+50%V_2O_5) showed the lowest weight loss compared to the base metal. Corrosion rate is less as compared to base metals due to low weight loss of weldment.

Major Findings: *Overall the Weldment should be the weight gain as compared to un-welded base material in case of molten (Na_2SO_4+V_2O_5) environment study. The high temperature oxidation resistance is not only related to the nature of the passive film, but it is also strongly dependent on the salt environment and the structure of the alloy.*

Keywords: *Austenitic Stainless Steel (ASS), Corrosion, GTAW Process, Inconel 718, Oxidation, Semi-Crystalline, X-Ray Diffraction Analysis*

**Author for correspondence*

1.0 Introduction

Manufacturing is one of the key sectors of any country's GDP and welding is one of the prime manufacturing processes of the manufacturing sector. It is used widely for fabricating different components like critical structures, boilers, pressure vessels, offshore structures, pipelines, aeroplane structures, rocket parts, nuclear environment components, automobiles, railways and electronic components etc. There are many welding methods or techniques commonly used for a wide range of applications. Welding process are most commonly carried out to joining of dissimilar metals, which have wide applications in the field of aero-space, gas turbine, boilers etc. In the below section is explained about challenges in dissimilar metal welding processes. Chuaiphan *et al*[1]. It was investigated that dissimilar metal TIG welding between Stainless Steel (SS 304) and low carbon steel (AISI 1020) is performed under the influence of an external magnetic field. Magnetic disturbances around the welding arc can cause arc instability, which can lead to lack of fusion, porosity, and uneven weld joints. An external magnetic field has a significant impact on the mechanical strength and quality of TIG welded joints. Jose Tom Tharappel *et al*[2], Inconel 718 is known for fusion zone cracking and liquidation cracking (micro fissuring) are serious defects in Inconel 718 welds. The Laves phase is the main culprit for cracks and the formation of these phases depends on the small grain size and composition of the base metal. Proper pre/post weld heat treatment reduces liquefaction cracks. Using elliptical oscillation methods to reduce these defects can reduce Nb segregation and the formation of laves. Jangra *et al*[3], reported that the bimetallic combinations of AISI 316 L and Inconel 718 obtained from orbital TIG welding were widely employed in the International Space station of Italy. Mithilesh *et al*[4]. The weldability, metallurgical, and mechanical properties of dissimilar joints of Inconel 625 and AISI 304 were investigated. Asymmetric joints were obtained by Gas Tungsten Arc (GTA) welding process using ERNiCrMo-3[5-7]. Successful welding of Inconel 625 and AISI 304 can be obtained by GTA welding process using ERNiCrMo-3. The corrosion is confined to the outer surface of the coating, forming thick layers of oxidants of Cr, Ni and their spinel oxides, which act as an extension of the transport of the coating rings Jeng *et al*[8].

2.0 Oxidation and Hot Corrosion

When alloys are used at elevated temperatures, they are undergoing inevitable oxidation and in some cases the formed oxide is protective so that further degradation of the material will be stopped or slowed down. However, if the working environment is too aggressive for the material, corrosion will take place of course, designers in industry would prefer if corrosion could be completely avoided and a lot of efforts have been put to improve corrosion properties, in different ways. The morphologies and types of oxides or corrosion products are greatly influenced by the environment. Commonly in industrial gas turbines blades, chromia, alumina, even sulfides, etc., form due to the very oxidizing hot exhaust gases, which also carries some impurities. Thus, understanding of the corrosion mechanisms in different environments will help to reduce the occurrence of corrosion.

Oxidation**:** When alloys are used in oxidizing environments, an oxide scale will form. The formation rate and the properties of the oxides determine whether the oxide scale is protective or not. In general, a protective oxide should be thin, dense, slowly growing, adherent to the metal, and thermodynamically stable within the working temperature range.

Hot Corrosion: In industrial processes, in addition to oxygen, the materials are also exposed to more aggressive environments, which contain mixed gases, molten salts, like alkali and sulfates, fly ashes and so on. At high temperatures, the interaction of these constituents with components results in accelerated oxidation or sulfidation attack finding, Hosseini *et al*[9]. This refers to high temperature corrosion or hot corrosion, which leads to a rapid degradation of materials. The three basic kinetic oxidation laws, described in 3.1.3, are also applicable for high temperature corrosion. The main difference is that the addition of salts makes the working environments more complex and usually the degradation becomes accelerated.Calvarin *et al*[10]. In general, based on the temperature range and the microstructure

formed, hot corrosion can be divided into two main types: High-Temperature Hot Corrosion HTHC (Type I) and Low-Temperature Hot Corrosion LTHC (type II).

3.0 Experimentation

This chapter addresses the experimental procedure carried out in assessing the mechanical and metallurgical properties of the dissimilar metal combinations of Inconel 718 and ASS 316. Metallurgical and mechanical examination was carried out using X-Ray Diffraction (XRD, to investigate the changes in the metallographic examination and the hot corrosion studies.

3.1 Composition of Base Materials

The Nickel and Ferrous based alloy materials selected for this study, viz. Inconel 718 and ASS 316 in the rolled sheet form. The chemical composition of the Inconel 718 and ASS 316 are reported in below table. The selected materials of Inconel 718 and ASS 316 are welded by using Gas Tungsten Arc Welding technique. The welding procedure of GTAW is discussed in the further sections.

3.2 GTA Welding

The specimens, with dimensions of ~30 ×25 ×3 mm^3, were cut from the alloy sheets of Inconel 718 and ASS316. Then the two pieces were joined by using the gas tungsten arc welding with suitable electrode (Non Consumable Tungsten Electrode). The welding specifications of GTAW are presented in Table 2. gas tungsten arc welding equipment and welding procedure as shown in Figure 1.

The spent electrode does not melt or deposit on the weld bed. The welded piece remains intact. Tungsten electrodes contain at least 99.10% tungsten and 0.80% zirconium. Zirconiated tungsten electrodes produce a very fixed arc and prevent tungsten sputtering.

3.3 Sample PreparationA

As shown in Figure 1, the welded part is separated into three pieces using diamond shaped cutter, the base metals and the weld portion metal is separate. The samples were then polished using emery papers of grit sizes 220, 400, 600 and then polished in grades 1/0, 2/0, 3/0 and 4/0. Final polishing was performed on a cloth polishing wheel machine with a 1 μm alumina powder suspension.first cleaned the samples with acetone and air-dried them

Table 1. Chemical composition of Inconel 718 and ASS 316

Element	Ni	Cr	Fe	Mo	Ti	Al	C	Si	S
Inconel 718 (Wt%)	53	17.5	Bal	3.13	0.97	0.51	0.03	0.1	0.002
ASS 316	10	18	Bal	2.0	0.80	0.04	0.08	1.0	0.03

Table 2. Specifications of GTAW

Welding Parameter (WP)	Peak Current (PC) (A)	Back-Ground Current (BGC) (A)	Speed(S) (mm/s)	Voltag (V)	Flow Rate (FR) (lit/ min)	Polarity (P)	Pulse Frequency (Pf)(Hz)	Heat Input(HI) (J/min)
Selection	75-140	37	3.5-4	50	8-10	DCEN	6	271

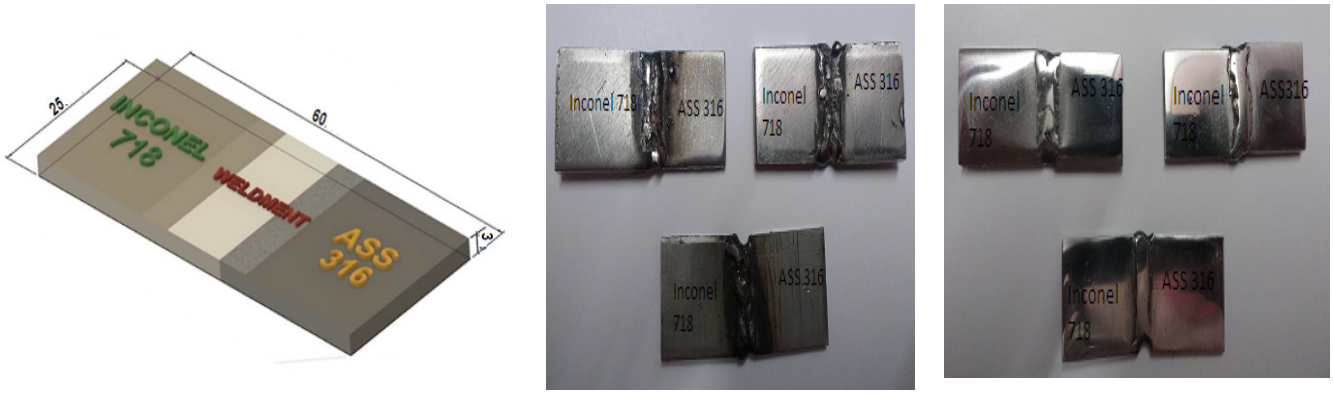


Figure 1. Dimensions of GTA welded specimens.

to remove any moisture on the sample, as shown in the Figure 1.

3.4 Experimental Process

Oxidation and hot corrosion studies were conducted in a laboratory muffle furnace at exposed temperatures ranging from 950^0 to 1150^{0}C. The Al_2O_3 boat was heated to 1200^{0}C for 6 hours, assuming that its weight remained constant during the study cycle.The welded part was cut into three pieces using a diamond cutter. Before proceeding to further studies, the samples were mirror polished with emery papers and also subjected to wheel cloth polishing for 5 minutes. After polishing the samples, we rinsed them clean, dried them in hot air to remove moisture, and measured the weight of the sample along with the boat before placing the sample in the boat holder and inserting it into the hot zone of the furnace. The time in the furnace was one hour, and after one hour the boat with the sample was taken out and cooled at ambient temperature for 20 minutes. The weight of the boat along with the sample was measured and it was noted that one cycle was completed here. Cyclic studies were conducted for the super alloy substrate in molten salt atmosphere (Na_2SO_4+50% V_2O_5) and 50 cycles in air. Each cycle consisted of one hour heating at different temperatures of 950^{0}C, 1050^{0}C and 1150^{0}C, in a muffle furnace.Then cool process for 20 minutes at room temperature like 28^{0}C. The main purpose of imposing cyclic conditions is to create a hot environment for hot corrosion testing. A uniform thickness coating of 3–5 mg/cm^2 (Na_2SO_4+50% V_2O_5) was applied to the preheated sample (250°C) using a camel hair brush. The difference in weights at the end of each cycle was measured using an electronic weight machine with a sensitivity of 1mg as shown in Figure 2. A Spelled scale was also included while measuring the weight change to determine the overall corrosion rate. The kinetics of corrosion were determined from the results of weight measurements. The samples after oxidation and hot corrosion were analyzed by XRD analysis for phase identification of the surface morphology (shown in Figure 3).

3.5 X-Ray Diffraction (XRD)

X-ray diffraction is very important for material classification. XRD is used for diffraction experiments to study the structural properties of materials at the molecular level. It is used to measure crystallinity and calculate lattice strain, chemical composition, order state, and determine phase diagrams.

3.5.1 Basic Principle

Compared to the spacing of crystal planes in a species, crystalline materials act as three-dimensional diffraction gratings for X-ray wavelengths. As shown in Figure 2 in a three-by-three crystal lattice, X-rays interact with electrons in atoms and are elastically scattered. Waves scattered from many atoms in a molecular plane can interfere with each other, and if the waves are in phase, they will interfere constructively. These diffracted X-rays contain information about the electron distribution in the materials. The diffracted beams are in specific

directions θ, is governed by Bragg's law, which relates the incident X-ray wavelength λ and the atomic plane spacing (d) as,

$$2d \sin\theta = n\lambda \quad (3.1)$$

The average crystallite size was determined by using Debye-Scherrer's equation.

$$d = \frac{0.89\lambda}{\beta cos\theta} \quad (3.2)$$

Where ;
d = Size of the Crystallite (nm)
λ =Wave length of X-ray used (1.5418A)
θ = Glancing angle (2θ/2)
β = Full width half maxima.

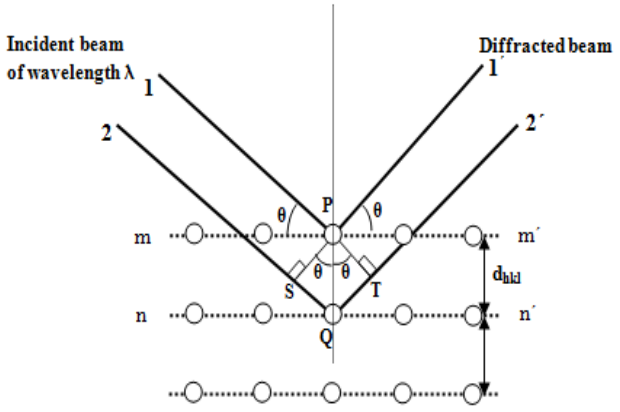


Figure 2. XRD crystallattice.

With the help of above techniques and apparatus discussed in this chapter, micro-structure micro-hardness and morphology of Inconel 718, ASS 316 and weldment metal are analyzed.

4.0 Results and Discussion

XRD Analysis: XRD analysis found that GTA welded dissimilar metals were exposed to various atmospheres of Na_2SO_4+ 50% V_2O_5 at 950°C to 1150°C and 50 cycles were shown in Figures 3-11. It is known that diffraction patterns identify heat-deteriorated welds in both environments. Fe_2O_3 is the main phase, Cr_2O_3, $NiCr_2O_4$, NiO, $Al_2Fe_2O_6$, Cr_3C_7, Cr_3Si & Mn_3Ni_2Si, weak peaks of ferrite and austenite are observed.

4.1 XRD Analysis at 950°C

The X-ray diffraction analysis of the Na_2SO_4 +50%V_2O_5 coated inconel 718, ASS 316 and weldment substrate at 950°C is as show in Figure 3, 4 and 5. The phases present in case of base metals and weldments are Inconel 718- Cr_2O_3, $NiCr_2O_4$, NiO, $Al_2Fe_2O_6$, Fe_2O_3, ASS 316-Austenite, Cr_3C_7, Cr_3Si and Mn_3Ni_2Si, Weldment- Ferrite, Austenite, and Cr_2O_3.

The corresponding phases are clearly seen on the base metals (Inconel 718, ASS 316) and weldment surface because of the uniform salt coating applied over the entire surface of the substrate. Strong peaks related to the matrix show that the scale is very thin or that little oxidation has occurred, and this result is the lowest parabolic rate constant for air oxidation. Protection from corrosion and oxidation is provided by the Cr_2O_3 layer but in the case of hot corrosion, the intensity of the peaks related to the matrix is very low. The major phases are identified in base metal of inconel 718 is Cr_2O_3, ASS 316 is Austenite and weldment is Ferrite[11,12].

4.1.1 X-ray Diffraction Pattern for Inconel 718 at 950°C

The diffraction pattern of Inconel 718 shows a cubic spinel phase with an FCC crystal structure without additional reflections and is well-referenced to the crystallographic

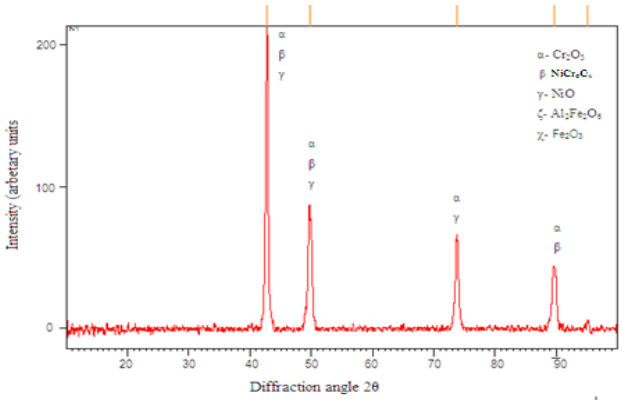


Figure 3. X-ray diffraction pattern for Inconel 718 exposed to cyclic oxidation in Na_2SO_4+ V_2O_5 environment at 950°C after 50th cycles.

planes of spinel Cr_2O_3, $NiCr_2O_4$, NiO, $Al_2Fe_2O_6$, F_2O_3, with 100% intensity at $2\theta = 42.7402^0$ that corresponds to the reflection plane $NiCr_2O_4$. The related parameters Full Width Half Maxima (FWHM), d-spacing and relative intensity with respective to each peak observed for Inconel 718 metal are listed. Determined the average particle size (by the D-S formula (Equation3.2)) is 12.09nm for pure Inconel 718; and decreasing content Inconel 718. As is clear from this figure, pure poly-aniline has a broad peak in the 40-760 region, with a maximum at 42.70 indicating its semi-crystalline nature. In Figure 3, as the content of Inconel 718 metal in the alloy increases, the relative intensity of the characteristic peaks of Inconel 718 nano alloys increases regularly, which clearly indicates the increase of Inconel 718 content in the alloys.

4.1.2 X-ray Diffraction Pattern for ASS 316 at 950^{0}C

Diffraction pattern of ASS 316 (Figure 4 also shows a cubic spinal phase the crystallographic planes of spinel Cr_3C_7, Cr_3Si and Mn_3Ni_2Si with 100% intensity at $2\theta=41.8476^0$ that corresponds to the reflection plane Cr_3Si. The related parameters Full Width Half Maxima (FWHM), d-spacing and relative intensity with respective to each peak observed for ASS 316 metal are listed. The average crystallite size was determined by Debye-Scherrer's formula (Equation 3.2) and for pure ASS 316 is found to be 8.582nm; and increases with decreasing content ASS

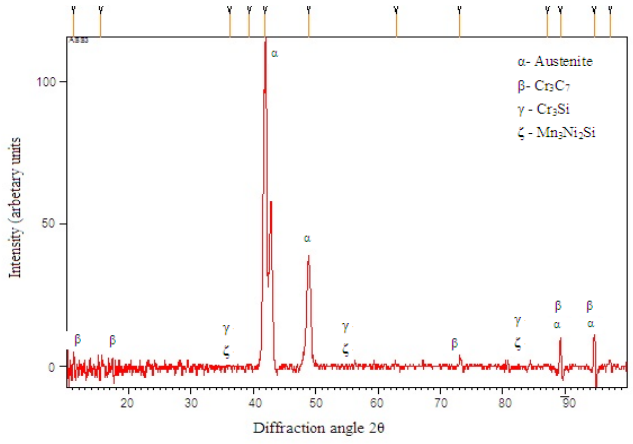


Figure 4. X-ray diffraction pattern for ASS 316 exposed to cyclic oxidation in Na_2SO_4+ V_2O_5 environment at 950^{0}C after 50th cycles.

316It is clear from this figure that pure polyaniline has a broad peak in the 41-520 region, with a maximum at 420, indicating its semi-crystalline nature. In Figure 4, as the content of ASS 316 metal in the alloy increases, the relative intensity of the characteristic peaks of ASS 316 metal alloys increases and decreases regularly, which clearly indicates a low increase in ASS 316 content in the alloys.

4.1.3 X-ray Diffraction Pattern for Weldment at 950^{0}C

Diffraction pattern of Weldment (Figure 5) shows the cubic spinel phase shows an FCC crystal structure without additional reflections and is well indexed to the crystallographic planes of spinel ferrite, austenite and Cr_2O_3 with an intensity of 100% at $2\theta=74.28790$, which corresponds to the reflection plane austenite. The related parameters Full Width Half Maxima (FWHM), d-spacing

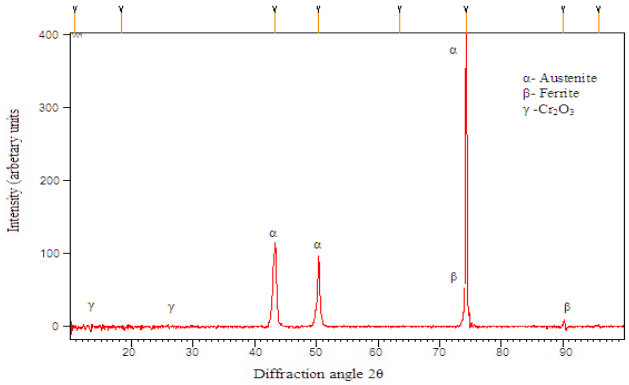


Figure 5. X-ray diffraction pattern for a weld subjected to cyclic oxidation in a Na_2SO_4+ V_2O_5 atmosphere at 950^{0}C after 50 cycles

and relative intensity with respective to each peak observed for Weldment metal are listed. The average crystallite size was determined by Debye-Scherrer's formula (Equation 3.2) and for pure Weldment is found to be 4.934nm; and increases with decreasing content Weldment. It is clear from this figure the region of 420 -760, with a maximum at 740 indicating its semi-crystalline nature. In the Figure 5 the relative intensity of the characteristic peaks of the welded composites increases and decreases regularly as the welding content in the composite increases, which

clearly indicates a low increase in the welding content in the composites. At 950^{0}C states, the weldment average crystallite size is very less compare to Inconel 718 and ASS 316 due to less intensity.

4.2 XRD Analysis at 1050^{0}C

The X-ray diffraction analysis of the Na_2SO_4 +V_2O_5 coated inconel 718, ASS 316 and weldment substrate at 1050^{0}C is as shown in Figures 6-8. The phases present in case of Inconel are Cr_2O_3, $NiCr_2O_4$, NiO, $Al_2Fe_2O_6$, F_2O_3, and ASS 316 are Austenite, Cr_3C_7, Cr_3Si and Mn_3Ni_2Si and that in weldment are Ferrite, Austenite, and Cr_2O_3. The phases are clearly seen on the surface of the base metals (Inconel 718, ASS 316) and Weldment due to the uniform coating applied to the surface of the substrate.

Strong peaks related to the matrix indicate that the scale is very thin or that little oxidation has occurred. The main phases identified are: Cr_2O_3, and $NiCr_2O_4$.

4.2.1 X-ray Diffraction Pattern for Inconel 718 at 1050^{0}C

Diffraction pattern of Inconel 718 (Figure 6) at 1050^{0}C shows a cubic spinel phase with FCC crystal structure without additional reflections and is well indexed to the crystallographic planes of spinel Cr_2O_3, $NiCr_2O_4$, NiO, $Al_2Fe_2O_6$, F_2O_3, with 100% intensity at 2θ = 42.4841^0 that corresponds to the reflection plane $NiCr_2O_4$. The related parameters Full Width Half Maxima (FWHM), d-spacing and relative intensity with respective to each peak observed for Inconel 718 metal are listed. The average crystallite size was determined by Debye-Scherrer's formula (Equation3.2) and for pure Inconel 718 is found to be 9.05nm; and decreasing content Inconel 718. As is clear from this figure, pure polyaniline has a broad peak in the 40-750 region, with a maximum at 420 indicating its semi-crystalline nature. In Figure4.2 (a), as the content of Inconel 718 metal in the alloy increases, the relative intensity of the characteristic peaks of Inconel 718 nano alloys increases regularly, which clearly indicates the increase of Inconel 718 content in the alloys.

4.2.2 X-ray Diffraction Pattern for ASS 316 at 1050^{0}C

Diffraction pattern of ASS 316 (Figure 7) shows cubic spinel phase with FCC crystal structure without additional reflections and spinel is well indexed to crystallographic planes of Cr_3C_7, Cr_3Si and Mn_3Ni_2Si, with 100% intensity at 2θ=43.0326^0 that corresponds to the reflection plane Cr_3Si. The related parameters Full Width Half Maxima (FWHM), d-spacing and relative intensity with respective to each peak observed for ASS 316 metal are listed. The average crystallite size was determined by Debye-Scherrer's formula (Equation 3.2) and for pure ASS 316 is found to be 10.2108nm; and increases with decreasing

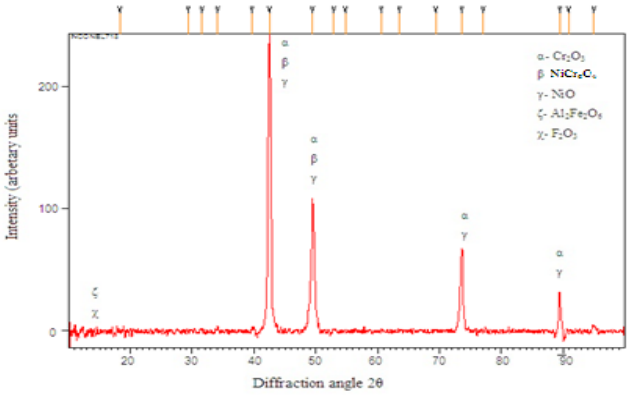


Figure 6. X-ray diffraction pattern for Inconel 718 exposed to cyclic oxidation in Na_2SO_4+ V_2O_5 environment at 1050^{0}C after 50th cycles.

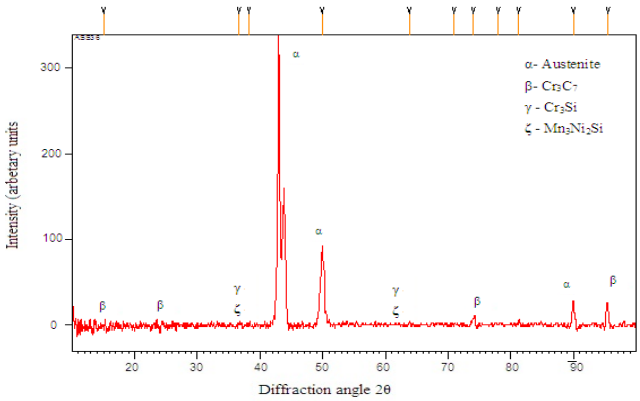


Figure 7. X-ray diffraction pattern for ASS 316 exposed to cyclic oxidation in Na_2SO_4+ V_2O_5 environment at 1050^{0}C after 50th cycles.

content ASS 316. It is a broad peak in the region of 41-530, with a maximum at 430, indicating its semi-crystalline nature in the Figure 7 with increasing content of ASS 316 metal in the composite the relative intensity of the characteristic peaks of ASS 316 metal composites increase and decreasing regularly, clearly indicating a less increase in the ASS 316 content in composites.

4.2.3 X-ray Diffraction Pattern for Weldment at 1050^{0}C

Diffraction pattern of Weldment (Figure 8) shows a cubic spinel phase with FCC crystal structure without additional reflections and is well-referenced to the crystallographic planes of spinel ferrite, Austenite,

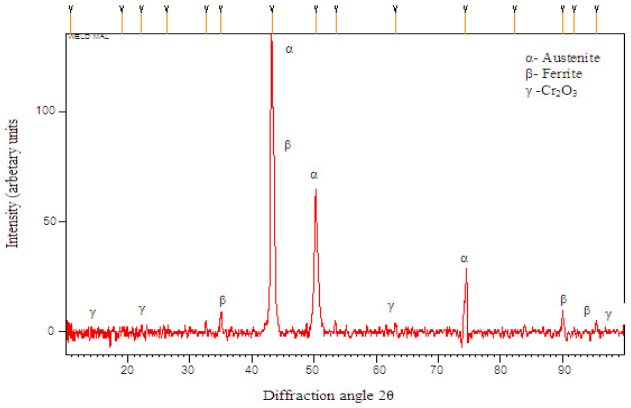


Figure 8. X-ray diffraction pattern for a weld subjected to cyclic oxidation in a Na_2SO_4+ V_2O_5 atmosphere at 1050^{0}C after 50 cycles.

and Cr_2O_3 with 100% intensity at 2θ=43.2566^0 that corresponds to the reflection plane Austenite. The related parameters Full Width Half Maxima (FWHM), d-spacing and relative intensity with respective to each peak observed for Weldment metal. The average crystallite size was determined by Debye-Scherrer's formula (Equation 3.2) and for pure Weldment is found to be 2.3490nm; and increases with decreasing content WeldmentIt is clear from this Figure 8, as the welding content in the composite increases, the relative intensity of the characteristic peaks of the welded composites increases and decreases regularly, which clearly indicates a low increase in the welding content in the composites.

4.3 XRD Analysis at 1150^{0}C

The X-ray diffraction analysis of the Na_2SO_4 +V_2O_5 coated inconel 718, ASS 316 and weldment substrate at 1150^{0}C show in Figure 9, 10, 11 The phases present in case of Inconel- Cr_2O_3, $NiCr_2O_4$, NiO, $Al_2Fe_2O_6$, F_2O_3, and ASS 316-Austenite, Cr_3C_7, Cr_3Si and Mn_3Ni_2Si and weldment- Ferrite, Austenite, Cr_2O_3. The present phases clearly show that base metals (Inconel 718, ASS 316) and Weldment material present over the surface and coating is applied uniformly over the entire surfaces of the substrate.

Strong peaks related to the matrix indicate that the scale is very thin or that little oxidation has occurred. Therefore, protection against corrosion and oxidation is provided by the Cr_2O_3 layer in the case. However, in the case of hot corrosion, the intensity of the peaks related to the matrix is much lower. The main phases identified are: Cr_2O_3, and $NiCr_2O_4$.

4.3.1 X-ray Diffraction Pattern for Inconel 718 at 1150^{0}C

Diffraction pattern of Inconel 718 (Figure 9) shows a cubic spinel phase with FCC crystal structure without additional reflections and is well-referenced to the crystallographic planes of spinel Cr_2O_3, $NiCr_2O_4$, NiO, $Al_2Fe_2O_6$, F_2O_3, with 100% intensity at 2θ = 45.6731^0 that corresponds to the reflection plane $NiCr_2O_4$. The related parameters Full Width Half Maxima (FWHM), d-spacing and relative intensity with respective to

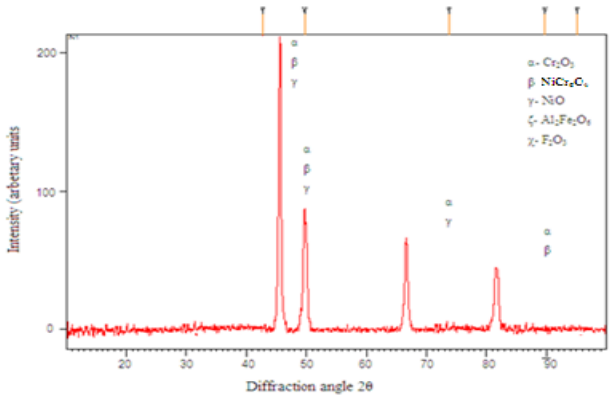


Figure 9. X-ray diffraction pattern for Inconel 718 exposed to cyclic oxidation in Na_2SO_4+ V_2O_5 environment at 1150^{0}C after 50th cycles.

each peak observed for Inconel 718 metal. The average crystallite size was determined by Debye-Scherrer's formula (Equation 3.2) and for pure Inconel 718 is found to be 10.9 nm; and decreasing content Inconel 718. As is clear from this figure, pure poly-aniline has a broad peak in the region of 42-830, with a maximum at 45.60 indicating its semi-crystalline nature. In Figure 9, as the content of Inconel 718 metal in the alloy increases, the relative intensity of the characteristic peaks of Inconel 718 nano alloys increases regularly, which clearly indicates the increase of Inconel 718 content in the alloys.

4.3.2 X-ray Diffraction Pattern for ASS 316 at 1150^{0}C

Diffraction pattern of ASS 316 (Figure 10) shows a cubic spinel phase with FCC crystal structure without additional reflections and is well-referenced to the crystallographic

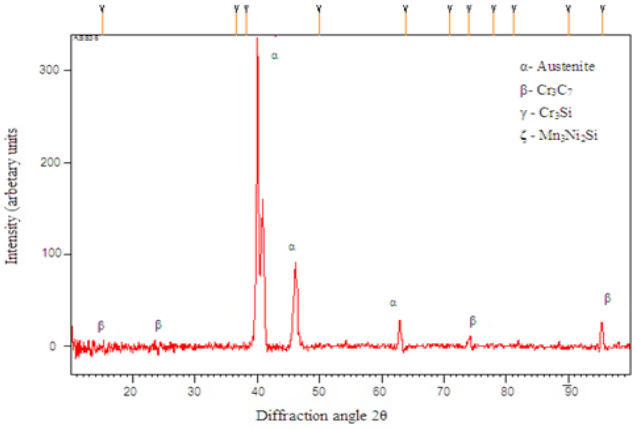


Figure 10. X-ray diffraction pattern for ASS 316 exposed to cyclic oxidation in Na_2SO_4+ V_2O_5 environment at 1150^{0}C after 50th cycles.

planes of spinel $Cr_3C_{7,}$ Cr_3Si and Mn_3Ni_2Si with 100% intensity at 2θ=40.009^0 that corresponds to the reflection plane Cr_3Si. The related parameters Full Width Half Maxima (FWHM), d-spacing and relative intensity with respective to each peak observed for ASS 316 metal are listed.The average crystallite size was determined by Debye-Scherrer's formula(Equation 3.2) and for pure ASS 316 is found to be 12.10nm; and increases with decreasing

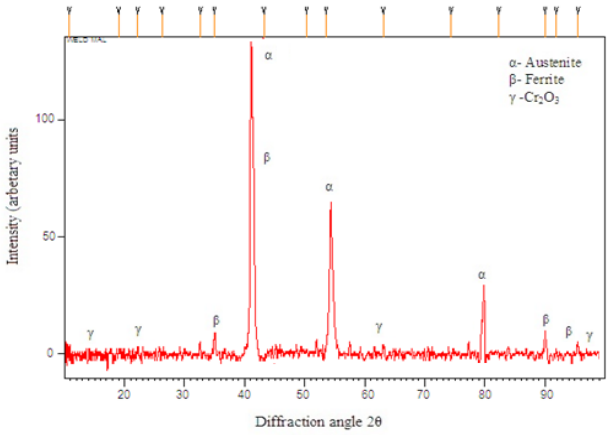


Figure 11. X-ray diffraction pattern for a weld subjected to cyclic oxidation in a Na_2SO_4+ V_2O_5 atmosphere at 1150^{0}C after 50 cycles.

content ASS 316. It is clear from this Figure 10 with increasing content of ASS 316 metal in the composite the relative intensity of the characteristic peaks of ASS 316 metal composites increase and decreasing regularly, clearly indicating a less increase in the ASS 316 content in composites.

4.3.3 X-ray Diffraction Pattern for Weldment at 1150^{0}C

Diffraction pattern of Weldment (Figure 1) shows a cubic spinel phase with FCC crystal structure without additional reflections and is well-referenced to the crystallographic planes of spinel Ferrite, Austenite, and Cr_2O_3 with 100% intensity at 2θ=45.3263^0 that corresponds to the reflection plane Austenite. The related parameters Full Width Half Maxima (FWHM), d-spacing and relative intensity with respective to each peak observed for Weldment metal are listed. The average crystallite size was determined by Debye-Scherrer's formula (Equation 3.2) and for pure Weldment is found to be 4.206nm; and increases with decreasing content Weldment. As is clear from this Figure 11, as the welding content in the composite increases, the relative intensity of the characteristic peaks of the welded composites increases and decreases regularly, which clearly indicates a low increase in the welding content in the composites.

4.4 Discussions

In the GTA welding the heat affected zone was observed. The welded samples, different from the scale, showed an outer layer containing Fe_2O_3, Cr_2Si, austenite, and $NiCr_2O_4$. XRD analysis was carried out for the base metals and the weldment at 950^{0}C, 1050^{0}C and 1150^{0}C and X-ray diffraction analysis indicated the formation of Cr_2O_3, $NiCr_2O_4$ and Fe_2O_3 phases which contributed to better corrosion resistance of the weldments. The present results are well in accordance with the findings as interpreted from XRD analysis on the as welded coupons is as shown in Figure 3 to 11. It was observed that the base metals Inconel 718 and ASS 316 had Cr_2O_3 and Austenite as major phases. Whereas, the weldment ferrite as the major phase. Debby-scherrers equation was used for calculating the average crystallite size. For this calculation the observations from XRD analysis were used (position of the phase, FWHM). The average crystallite size was determined for base metals; weldment and the values were compared. It was found that average crystallite size was less as compared to the base metals which implies weldment has good corrosion resistance.

5.0 Conclusions

The conclusions from the present study on gas tungsten arc welding and base metal with molten salt (Na_2SO_4+50%V_2O_5) atmosphere are summarized here, Gas Tungsten Arc Welding (GTAW) has been successfully used to join dissimilar alloys like Inconel 718 and ASS 316. This difference in hardness is due to the formation of carbides during the welding thermal cycle. Molten salt (Na_2SO_4+50%V_2O_5) showed the least weight loss compared to the TIG welding base metal in environmental studies. XRD analysis identification is the presence of Fe_2O_3 as the main phase in the hot corrosion environment. In XRD analysis the weldment average crystallite sizes is very less as compared to Inconel 718 and ASS 316. TIG weldments show the parabolic behaviour in the molten salt environment, as far as the corrosion kinetics is concerned[13]. The weldment shows higher resistance to oxidation and hot corrosion compared to Inconel 718 and ASS 316 under given environmental conditions at 950^{0}C, 1050^{0}C and 1150^{0}C. The improved performance of welding in both environments is attributed to the tendency of chromium and nickel and their spinel to form protective oxides. The less protective oxide of iron is abundant in surface scale formation and accounts for the relatively low oxidation resistance of Inconel 718 and ASS 316.The surface scale, rich in iron oxides and iron and nickel sulphides, contributed to its poor hot corrosion resistance in a given environment.

6.0 References

1. Chuaiphan W, Somrerk CA, Niltawach S, Sornil B. Dissimilar welding between AISI 304 stainless steel and AISI 1020 carbon steel plates. J Appl Mech. 2012. https://doi.org/10.4028/www.scientific.net/amm.268-270.283
2. Tharappel JT, Babu J. Welding processes for Inconel 718- A brief review. IOP Conference Series Materials Science and Engineering.2018; 330:012082. https://doi.org/10.1088/1757-899x/330/1/012082
3. Jangra KK, Sharma N, Khanna R, Matta D. An experimental investigation and optimization of friction stir welding process for AA6082 T6 (cryogenic treated and untreated) using an integrated approach of Taguchi, grey relational analysis and entropy method. Proceedings of the Institution of Mechanical Engineers Part L Journal of Materials Design and Applications. 2015; 230(2):454–469. https://doi.org/10.1177/1464420715578182
4. Mithilesh P, Varun D, Reddy ARG, Ramkumar KD, Arivazhagan N, Narayanan S. Investigations on dissimilar weldments of Inconel 625 and AISI 304. Procedia Engineering. 2014; 75:66–70. https://doi.org/10.1016/j.proeng.2013.11.013
5. Dehmolaei R, Shamanian M, Kermanpur A. Factors affecting weldability Improvement of dissimilar welds of aged HP stainless steel and alloy 800; 2008. http://journal.issiran.com/article_4833.html
6. Hong C, Gu D, Dai D, Alkhayat M, Urban W, Yuan P, Cao S, Gasser A, Weisheit A, Kelbassa I, Zhong M, Poprawe R. Laser additive manufacturing of ultrafine TiC particle reinforced Inconel 625 based composite parts: Tailored microstructures and enhanced performance. Mater Sci Eng A. 2015; 635:118–128. https://doi.org/10.1016/j.msea.2015.03.043
7. Sridhar R, Ramkumar KD, Arivazhagan N. Characterization of microstructure, strength, and toughness of dissimilar weldments of Inconel 625

and duplex stainless steel SAF 2205. Acta Metall Sin (English Letters). 2014; 27(6):1018–1030. https://doi.org/10.1007/s40195-014-0116-5

8. Jeng SL, Lee HT, Weirich TE, Rebach WP. Microstructual study of the dissimilar joints of Alloy 690 and SUS 304L stainless steel. Mater Trans. 2007; 48(3):481–489. https://doi.org/10.2320/matertrans.48.481
9. Hosseini HS, Shamanian M, Kermanpur A. Characterization of microstructures and mechanical properties of Inconel 617/310 stainless steel dissimilar welds. Mater Charact. 2011; 62(4):425–431. https://doi.org/10.1016/j.matchar.2011.02.003
10. Calvarin G, Molins R, Huntz AM. Oxidation mechanism of NI—20CR foils and its relation to the Oxide-Scale microstructure. Oxid Met. 2000; 53(1/2):25–48. https://doi.org/10.1023/a:1004578513020
11. Knutsson P, Lai H, Stiller K. A method for investigation of hot corrosion by gaseous Na_2SO_4. Corros. Sci. 2013; 73:230–236. https://doi.org/10.1016/j.corsci.2013.04.006
12. Rapp RA. Hot corrosion of materials: a fluxing mechanism? Corros. Sci. 2002; 44(2):209–221. https://doi.org/10.1016/s0010-938x(01)00057-9
13. Sidhu T, Malik A, Prakash S, Agrawal R. Cyclic oxidation behavior of Ni- and Fe-based superalloys in air and Na_2SO_4-25%NaCl molten salt environment at 800°C. Int J Phys Sci. 2006; 1(1):27–33. https://doi.org/10.5897/ijps.9000148